STUDY OF THE INFLUENCE OF MATERIAL PROPERTIES ON RESIDUAL STRESS IN SELECTIVE LASER MELTING

B. Vrancken[1], R. Wauthle[2,3], J.-P. Kruth[2], J. Van Humbeeck[1]

[1]Department of Metallurgy and Materials Engineering, KU Leuven, Leuven, Belgium
[2]Department of Mechanical Engineering, KU Leuven, Leuven, Belgium
[3]LayerWise NV, Leuven, Belgium
Accepted August 16th 2013

Abstract

Selective laser melting (SLM) is characterized by highly localized heat input and short interaction times, which lead to large thermal gradients. In this research, nine different materials are processed via SLM and compared. The resulting microstructures are characterized by optical and scanning electron microscopy. Residual stresses are measured qualitatively using a novel deflection method and quantitatively using X-ray diffraction. Microcracking, surface oxidation and the anisotropy of the residual stress are discussed. The different phenomena interacting with the buildup of residual stress make it difficult to distinguish the possible correlations between material parameters and the magnitude of residual stresses.

Introduction

In Selective Laser Melting (SLM) a high power laser locally melts successive layers of powder to produce complex shape 3D metal parts. The highly localized heat input leads to fast melting and solidification, resulting in a unique microstructure. SLM possesses several advantages over other production techniques, such as limited material loss, a high level of flexibility and near net shape production of geometrically complex functional parts. The process details and applications have been widely reviewed elsewhere, and the reader is referred to Ref [1] for more details.

However, several disadvantages and difficulties still limit the potential of the SLM process to produce large or complex parts from any type of material. The localized heat input and fast solidification lead to large thermal gradients, both in time and space. Firstly, differences in thermal shrinkage lead to a large buildup of thermal stresses, which can cause premature failure of the part by macro- or microcracks and delaminations. In larger parts, residual stress works over larger dimensions, making these parts more prone to this type of failure. Secondly, dimensional accuracy can be negatively influenced by deformation and warping of the part, especially after removal from the base plate. Thin walled sections (less than 0.5 mm thick), overhang structures and any other type of geometry that possesses low geometrical stiffness suffer most from these deformations. Lastly, the residual stress, which is usually tensile in nature at the surface, can lower the effective structural loads that parts can carry.

Because modeling of a thin wall reduces the problem from 3D to 2D, early research efforts have mainly focused on thin walls built via Laser Engineered Net Shaping or LENS®. Vasinonta *et al.* [2, 3] created process maps using non-dimensional variables to link process parameters to the melt pool size and thermal gradients in the steady state region of the wall. Using uncoupled thermomechanical FE analysis, these gradients were linked to stresses in a thin

304 stainless steel wall. Aggarangsi *et al.* [4] focused on the non-steady state edges of the walls, where melt pool size was seen to increase and large tensile stresses in the Z-direction are built up, compensated by compressive stresses in the center of the wall. Although only the top layer of a 316L SS thin wall was modeled, they showed that reducing the laser power when approaching the free edge stabilizes the melt pool depth but that this does not influence the residual stresses at the free vertical edges. The main cause hereof was found to be the contraction of the upper layer, which is constrained by the substrate below. These results were corroborated by Zekovic *et al* [5], whose models showed vertical tensile stresses in the region near the base exceeding the yield stress. Experiments revealed cracks at these locations, validating the model.

Rangaswamy *et al.* [6] and Moat *et al.* [7] both used neutron diffraction and the contour method to experimentally quantify the stresses in beam shaped parts produced by LENS®. Large vertical tensile stresses at the sides are balanced by compressive stresses in the center of the part. The deposition pattern or scan strategy was found to be very important for 3D structures. In this light, Klingbeil *et al.* [8], Mercelis and Kruth [9] and others [10, 11] proposed to minimize the length of the scan vectors, for instance by dividing the area to be scanned in smaller sectors, a strategy called island scanning. Lastly, many authors have proposed that preheating lowers thermal gradients and the magnitude of residual stress [8, 9, 12, 13].

While research has mainly focused on the influence of deposition patterns, it has focused less on the individual effects of process parameters and even less on the effects of material properties on the final magnitude and distribution of the residual stresses inside SLM parts. In this paper, nine different materials are compared via XRD stress measurements, deformation of bridge-shaped parts and FE calculations to distinguish a correlation between the material properties and the final residual stress state.

Materials and methods

All the materials that are studied in this research are listed in Table 1 together with all the relevant material properties that are used for comparison. All material properties listed are values at room temperature. Production of samples took place at the PMA division of the department of Mechanical Engineering of the KU Leuven or at LayerWise NV (Leuven, Belgium). Process parameters were chosen to achieve maximum values for density. All parts except those made of 316L, 18Ni300 maraging steel, Inconel 718 and Hastelloy C-276 were produced with an identical scanning strategy, layer thickness. 316L, 18Ni300 maraging steel, Inconel 718 and Hastelloy C-276 parts were produced with identical scanning strategy, layer thickness and process parameters. Parts were removed from the base plate via wire electro discharge machining.

Density was measured using the Archimedes technique. An Axioskop 40 Pol/40 A Pol light optical microscope and Philips XL30 FEG scanning electron microscope (SEM) were used to investigate microstructure and the as built top surface. Vickers microhardness was measured with a Leitz-Durimet microhardness tester using a weight of 300 g for 10 seconds.

To analyze residual stresses, a novel qualitative method was used. In the Bridge Curvature Method or BCM [14], three bridge shaped parts (as depicted in Figure 4) are built per material. After removal from the base plate, the stresses inside the bridge are partially relaxed and the bridge curls up to a certain angle, giving information about the residual stresses. The curl-up

angle α is a semi-quantitative indicator of the magnitude of the residual stress inside the part. However, by applying the angle of deformation to a finite element (FE) model of the bridge, quantitative values for the stresses can be calculated. The angle of deformation α is measured using a Mitutoyo Quick Vision Pro 202 optical coordinate measuring machine, and stresses were calculated using the commercially available ABAQUS FE package.

In addition to the BCM method, residual stresses in the top layer of 10x10x10 mm³ cubes were measured by XRD using a Siemens D500 with Cu radiation with a wavelength of λ_{Cu} = 1.542Å or a Seifert MZ4 with Cr radiation with a wavelength of λ_{Cr} = 2.29Å. Since the accuracy of XRD stress measurements increases for higher values of 2θ, the selection of a suitable peak was the criterion for the choice of radiation. X-ray elastic constants were calculated from values of the single crystal elastic constants available in literature using the Voight-Reuss-Hill model.

Table 1 List of material properties [15-18]

Material	Material properties										
	Thermal expansion	Thermal conductivity	Specific heat capacity	Thermal diffusivity	Density	Melting point	Vickers hardness	Yield stress	Ultimate Tensile Strength	Young's modulus	Poisson ratio
	α	k	Cp	Df	ρ	Tm	Hv	$\sigma_{0,2}$	UTS	E	ν
	10^{-6}/K	W/(m.K)	J/(kg.K)	10^{-6} m²/s	kg/m³	K	0.3; 10s	MPa	MPa	GPa	
Ti Grade 1	9.4	16	520	6.82	4510	1943	225	572	629	96	0.320
Ti6Al4V-ELI	10.1	6.7	930	1.63	4430	1933	399	1050	1140	111	0.320
316L	18.6	21.5	500	5.41	7950	1648	230	500	635	170	0.285
Maraging18Ni300	11.3	15	450	4.12	8100	1686	388	100	1100	180	0.300
Ta	6.5	54.4	139.1	23.45	16680	3269	225	463	513	185	0.360
W	4.5	173	130	69.13	19250	3695	395	1600	1725	400	0.280
Inconel 718	16	11.4	450	3.08	8220	1533	347	634	980	170	0.284
AlSi10Mg	23	113	963	43.95	2670	868	138	275	445	70	0.330
Hastelloy C-276	13.4	19	427	5.03	8840	1644	295	351	620	205	0.320

Results

Density

The relative densities for all materials have been summarized in the first column of the measurements section in Table 2. It can be seen that all relative densities are higher than 99%, except for 18Ni300 maraging steel, W, AlSi10Mg and Hastelloy C-276. Porosity is an important factor in the final residual stress state, as the pores are stress free zones in a highly stressed material, causing relaxation in the direct vicinity of the porosity. For W (Figure 1) and Hastelloy C-276 (Figure 2), the lower density values can be explained by microcracking and in the case of W also by large irregular pores. These pores and cracks are also the cause of the relatively low Vickers hardness of the W samples. Improper build conditions during the AlSi10Mg build led to large irregularly shaped pores. These conditions were likely caused by an unacceptable concentration of oxygen during the build. However, fairly spherical, large pores are also present. The abnormal build conditions might have caused the melt pool to be more unstable than usual, leading to larger fluctuations in size and depth of the melt pool. As Thijs *et al.* [19] have shown

for AlSi10Mg, this material is prone to the formation of large pores when melting conditions fluctuate and become similar to keyhole welding. This can cause the melt pool to collapse, trapping gas bubbles. These pores are called keyhole pores. Other than the low density, the bad build conditions for AlSi10Mg resulted in a poor surface quality, as will be shown further in Figure 6A. The origin and the influence of cracks will be discussed later in the text.

Microstructure

While it is outside the scope of this paper to discuss all the different structures in detail, some remarks are made that are relevant to the residual stress. In W, microcracks appear along the grain boundaries, visible in Figure 1B and Figure 6H. In the top views, these grains are seen to be confined to the track width. The individual grains have an S-shape similar to SLM microstructures previously observed for pure Ta [20] and in welds. The origin of these S-shaped grains is the local temperature gradient across the scan track. Along the midline of the scan tracks and at the back of the moving melt pool (where the material solidifies), the thermal gradient is the largest in the scan direction, so grains will tend to grow in this direction. Moving from the midline to the edge of the melt pool, the maximum thermal gradient rotates and at the edge, is perpendicular to it. However, due to the overlap of scan tracks, part of the scan track is remolten, and the grain is partially remelted. Due to the fast cooling conditions, the grains grow epitaxially towards the center of the new melt pool, where thermal gradients are again parallel to the scan direction, which is rotated 180°C compared to the adjacent scan track due to the zigzag scanning strategy. The final outcome is an S-shaped grain spanning the centers of adjacent tracks. The ends point along the center of adjacent melt tracks, in the opposite direction of the laser movement. In the side view (Figure 1A), these cracks are less obvious and large, irregularly shaped pores are visible.

By contrast, in the Hastelloy C-276 sample, the grain boundaries are not as clear from the crack pattern and the cracks seem to resemble the scan strategy, as seen in the top view in Figure 2. This results in a rough hexagonal crack pattern. In the side view, the vertical cracks are straight with sharp corners, resembling a lightning shape. The cracks are not oriented perfectly parallel with the build direction but under a slight angle.

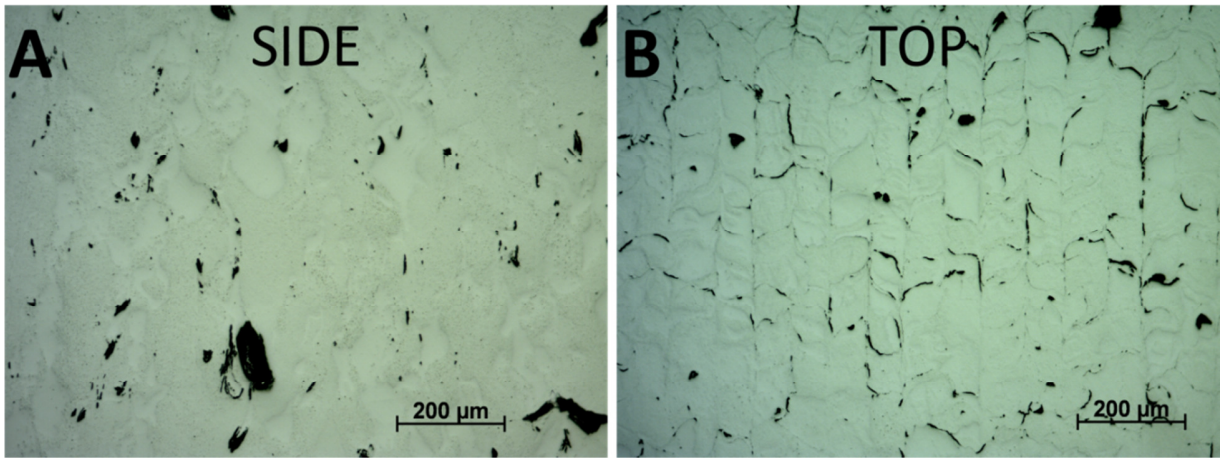

Figure 1 Microstructure of W after SLM. (A) Side view, with large irregular shaped pores. The build direction is vertically upward. (B) Top view, with cracking along grain boundaries. The scan tracks in this section are oriented vertically.

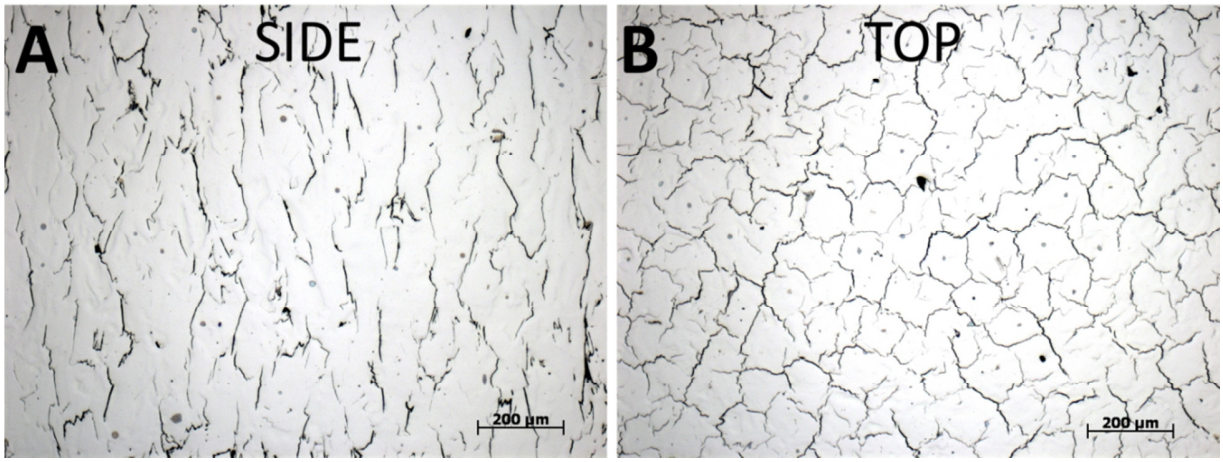

Figure 2 Microstructure of Hastelloy C-276 after SLM. (A) Side view. The build direction is vertically upward. (B) Top view. The black lines are not grain boundaries but cracks.

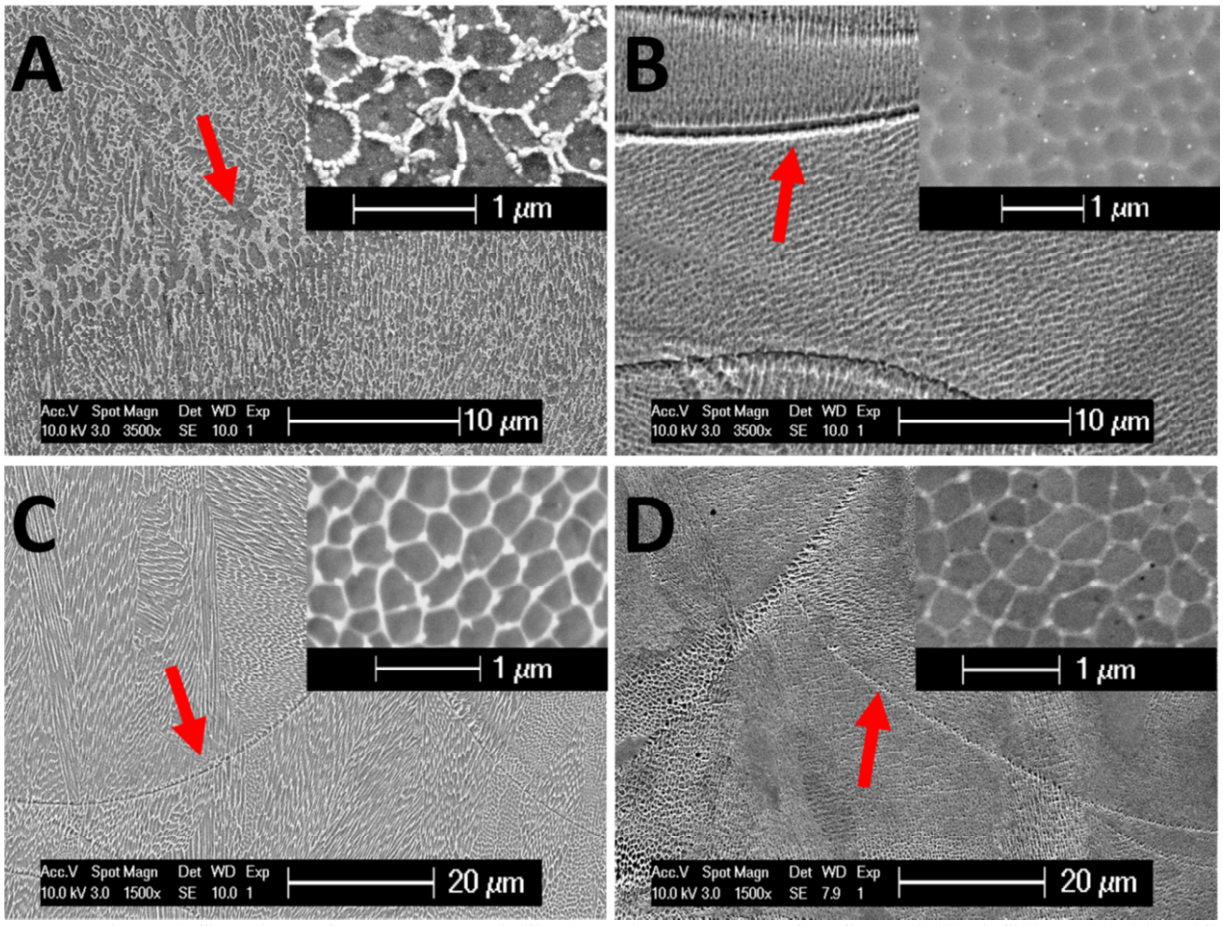

Figure 3 Side views of the cellular solidification microstructures after SLM of (A) AlSi10Mg (B) 316L (C) Maraging 18Ni300 steel and (D) Inconel 718. Top views, perpendicular to the cell growth direction are inserted at the right upper corners. The red arrows indicate melt pool boundaries in the side views.

AlSi10Mg, Inconel 718, maraging steel and 316L all have a similar solidification structure, wherein the local thermal gradients inside the melt pool are the most important factor.

An overview for these four materials is given in Figure 3. Solidification occurs in a cellular/dendritic fashion with the growth direction preferably oriented towards the center of the melt pool. The fast and directional solidification leads to a very fine and homogeneous intercellular spacing of less than 1 µm, contributing to excellent strength and hardness. These cells are not individual grains but constitute a substructure inside one grain. Grains are defined by a group of adjacent cells that grew in the same crystallographic direction. While the cells are directly adjacent to one another in Inconel 718, maraging steel and 316L, a very fine eutectic is formed between the primary aluminum grains in AlSi10Mg with a lamellar spacing of less than 100 nm. The red arrows indicate the melt pool boundaries in the side views. While this is a fine, well defined line for 316L, Inconel718 and maraging steel, it is a somewhat diffuse zone for AlSi110Mg in which the microstructure is slightly coarser.

The microstructure of Ti6Al4V after SLM has been widely discussed in literature [21-23] and consists of acicular α' martensite inside prior β grains. TiCP1 has a similar acicular α' structure, but prior β grains are not clearly distinguishable.

Residual stress

The average curl-up angle α (see Figure 4) of the three bridges for each material is given in the second column of the measurements section of Table 2. The values range from 0.15 ± 0.06° for W to 1.53 ± 0.11° for Inconel 718. Because the angle of deformation is closely related to material properties such as the stiffness and yield stress, the absolute value of the curl-up is only significant when comparing the same material which is produced using different scanning strategies or process parameters. However, when the deformations are inserted into a finite element (FE) model of the bridge using material specific properties, a quantitative value is obtained for the stress state needed to deform the bridge to the measured angle. Assuming identical behavior in tension and compression, the deformation is applied to a stress free, undeformed model of the bridge. The resulting stress field inside the deformed bridge is then the opposite of that needed to make the bridge curl up.

While the model is too simple to take the resulting local stress values as correct, it is more likely that the model gives an accurate estimate of the stress gradient between the top of the part, at point A, and the top of the underside of the bridge, at point B two millimeters lower. After all, it is mainly the stress gradient between these two locations that makes the bridge curl up to the measured angle. Values for this gradient are given in the last column of Table 2. The gradients are very large and vary between 202 MPa for maraging steel to 1267 MPa for Inconel 718 or an equivalent gradient of around 634 MPa/mm. It is clear that such large gradients can lead to heavy deformations.

Apart from the stress analysis via the BCM method, residual stresses were also measured on the top surface via XRD. Results are summarized in the third and fourth column of the measurements section of Table 2. Both the maximum stress and the minimum principal stress are reported. The severe cracking of the W samples is reflected by the low value of residual stress and low curl-up angle. The measured XRD stress of -34 ± 15 MPa can be assumed negligible compared to the expected yield stress of W of around 1600 MPa. Hastelloy C-276 is also heavily cracked, but the resulting curl-up angle of 0.90 ± 0.19° is the result of significantly large stresses. Furthermore, at 358 ± 14 MPa, the stress in the top layer is close to the yield stress found in literature. This will be further discussed under 'Cracking' in the Discussion section.

The bridges made from maraging 18Ni300 steel also show very limited curl-up, and XRD measurements of the cube specimen show compressive stresses at the top. This is contradictory to the consensus in literature that residual stresses in SLM parts are tensile on the outer surfaces and compressive in the bulk.

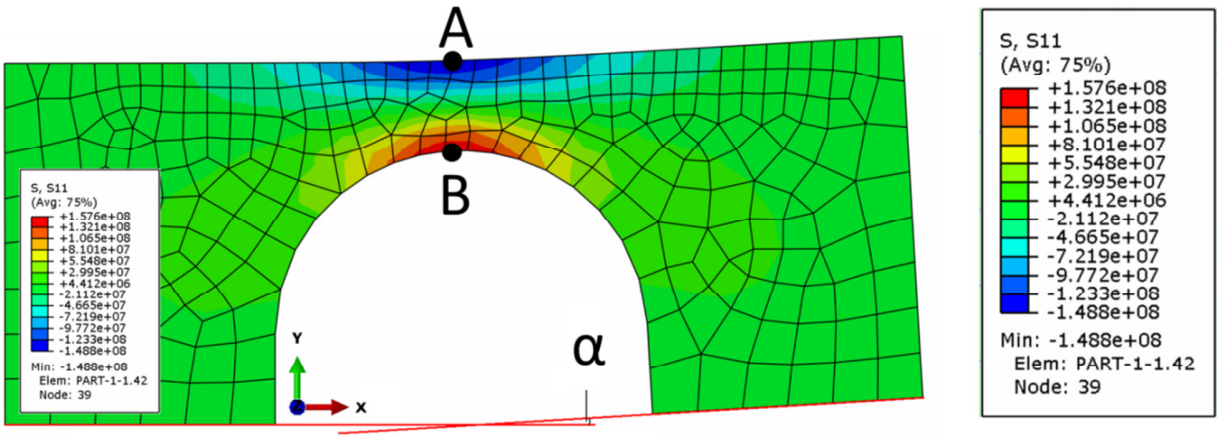

Figure 4 Stress state of an originally stress free, deformed bridge specimen, shown for Ta but similar for all other materials.

Table 2 Overview of density, deformation angle, measured maximum stress and calculated stress to cause the measured deformation for each material.

Material	Measurements				Calculations	
	Density	BCM deformation	X-ray principal stresses		FE model	
	Archimedes		Maximum σ_1 (in absolute value)	Minimum σ_2	Top BCM before curl-up	Stress gradient (A-B)
Name	%	°	MPa		MPa	
Ti Grade 1	99.7 ± 0.3	0.87 ± 0.06	222 ± 10	101 ± 10	216	445
Ti6Al4V-ELI	99.3 ± 0.2	1.29 ± 0.07	406 ± 25	119 ± 20	351	723
316L	99.6 ± 0.1	0.77 ± 0.04	-68 ± 3	-15 ± 3	352	724
Maraging 18Ni300	98.0 ± 0.4	0.23 ± 0.11	-263 ± 13	-138 ± 13	98	202
Ta	99.6 ± 0.1	0.34 ± 0.08	197 ± 24	85 ± 24	149	306
W	98.0 ± 1.7	0.15 ± 0.06	-34 ± 15	24 ± 15	144	296
Inconel 718	99.3 ± 0.2	1.53 ± 0.11	419 ± 15	296 ± 15	615	1267
AlSi10Mg	98.2 ± 0.6	0.78 ± 0.07	64 ± 3	55 ± 3	129	266
Hastelloy C-276	97.6 ± 0.6	0.90 ± 0.19	358 ± 14	98 ± 14	436	899

Discussion

Correlation between material properties and stress

Solidification theory states that materials with a small thermal diffusivity *Df* are more prone to develop large thermal residual stresses [24]. These materials retain a lot of heat due to their high specific heat capacity *Cp* and do not conduct the heat away effectively due to their low thermal conductivity *k*. This leads to large thermal gradients inside the part, and consequently to large strain gradients and large residual stresses. However, when plotting the maximum principal stress and curl-up angle against the thermal diffusivity in Figure 5A, it is impossible to distinguish this trend from the data.

A large thermal expansion coefficient means that the shrinkage of the material during cooling will be large. Because this shrinkage is constrained by previously deposited material, larger shrinkage should lead to larger stresses. As a simplistic example, consider the shrinkage in the longitudinal direction of a scan track of L = 1 cm length of 316L and of maraging steel. Assume the thermal expansion to be constant and equal to the value at room temperature. Both materials have a similar melting temperature. The total unconstrained shrinkage of 316L would be equal to $\Delta L_{316L} = \alpha_{316L}.L.\Delta T_{316L}$ = 221 µm, where ΔT_{316L} is the difference between the melting temperature and room temperature. For maraging steel, the shrinkage is $\Delta L_{Mar} = \alpha_{Mar}.L.\Delta T_{Mar}$ = 157 µm. This demonstrates the theoretical effect of the thermal expansion on residual stress build up. Because the thermal expansion coefficient is not constant and goes up with rising temperature, these absolute values for the unconstrained shrinkage are an underestimation.

The same formula also describes the effect of the melting temperature. Comparing AlSi10Mg and Ti6Al4V, the unconstrained shrinkage of the Al alloy would be equal to ΔL_{Al} = 120 µm, while that of Ti6Al4V would be $\Delta L_{Ti6Al4V}$ = 132 µm, even though the thermal expansion coefficient of AlSi10Mg is much larger than that of Ti6Al4V. Because Ti6Al4V solidifies at much higher temperatures, shrinkage occurs over a larger temperature range and stresses can develop to a larger extent during cooling.

However, the shrinkage is constrained and assumed to be small in a real SLM part. The theoretical shrinkage can then be converted to strains and, using the Young's modulus, to stresses, assuming all deformations are elastic. Performing this calculation for all materials, this would mean that the final stress in one scan track is much higher than the yield stress at room temperature, which is unrealistic. For instance, the stress inside a Ti6Al4V track would amount to 1.49 GPa. This means that the material will yield due to the residual stress at some point during cooling. The temperature at which the material yields depends on the total amount of virtual shrinkage that has already taken place and the value of the yield stress at that temperature. Thus, the value of the yield stress at high temperature is also important, as it limits the maximum value of the residual stress.

Again, plotting the measured maximum principal stress and curl-up against the various material parameters mentioned above in Figure 5, no clear trends could be distinguished. Using combinations of material properties on the x-axis or scaling the measured stress with the yield stress does not result in better correlations. Various phenomena obscure the influence of the material parameters, such as microcracking, the formation of oxides and porosity. Furthermore,

because all samples were built according to predetermined parameters to obtain high density, a wide range of parameters and energy densities were used in this research. The influence of the process parameters is not yet fully understood and may be a dominant factor over the material properties.

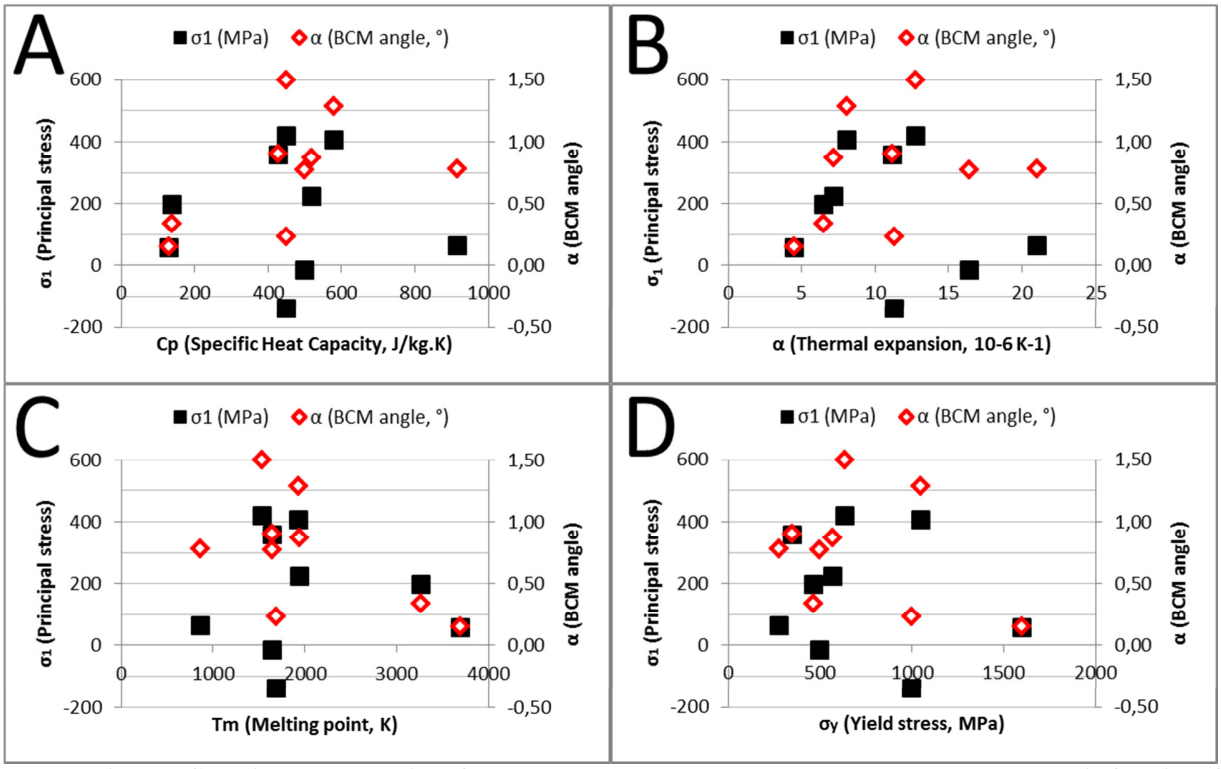

Figure 5 Graphical representation of the stress related measurements, σ_1 and the curl-up angle α in function of selected material properties.

Direction of principal stress

Figure 6 shows all the as built top surfaces of the cube samples. In Figure 6A, the bad surface quality of the AlSi10Mg sample is shown. The center of the image shows a deep, circular hole in the middle of a scan track. This is a typical keyhole pore. This surface is not characteristic of the normal surface quality for AlSi10Mg but is shown to indicate the direction of residual stresses. All other surfaces can be divided into two groups. In the first group, image B to G, the melt pool contours are very elongated and have a pointed tail. This particular shape of the melt pool is characteristic for conditions in which a high speed is used and has been observed before in high speed welds. The second group consists of Ta and W, for which the melt pool contours are clearly more rounded. A very high energy input is needed to melt these metals because of their high melting temperature.

By measuring the stress in three different directions, the full stress tensor at the location of the measurement can be calculated. The assumption is made that the stress perpendicular to the surface is zero and that a plane stress situation is present on the top surface. Because the penetration depth of X-rays into the material is typically a couple of tens of micrometers, only the stress in the last scanned layer is measured. Due to the plane stress assumption, only two

principal stresses are nonzero. σ_1 is the upper limit of the stress and σ_2 the lower limit. Both stresses are perpendicular to each other and are reported in Table 2. The shear stresses in the principal stresses coordinate system are negligible. The difference between σ_1 and σ_2 is large and clearly illustrates the anisotropic nature of the residual stress build up. The red double arrow in the right upper corner of each image indicates the direction of the largest principal stress (σ_1) in the top layer. Remarkably, this direction almost perfectly coincides with the direction of the scan vectors of the last layer for all materials. Early research on residual stresses in AM parts has shown that the stresses are largest in the direction of the scan vectors [8-11]. This principle has led to widely adopted scan strategies such as island scanning in which the lengths of the scan vectors are reduced to minimize problems with residual stresses.

As the melt pool solidifies and cools, it will tend to shrink in all directions. However, the narrow width of the melt pool means that shrinkage in the transversal direction is small, and the major amount of shrinkage will tend to occur in the longitudinal direction. The colder and stronger material of the previous layers will restrain this contraction, leading to the development of large longitudinal stresses.

As a reminder, the stresses are measured at the top of 10x10x10 mm³ cubes. It is expected that these values will increase for larger samples and reach a certain maximum stress level. At what minimum size this plateau is reached is subject of future research.

Cracking

In Figure 1, the extensive cracking of SLM W parts is shown. The cracks form a linked network and are all located on the grain boundaries, with the majority of cracks oriented along the scan direction in the middle of the scan track. Because W is a BCC material, it has a ductile to brittle transition temperature (DBTT). The high melting point of W means that the DBTT is above room temperature. Plastic deformation is almost non-existent for temperatures below 200°C, while good ductile behavior usually only starts at temperatures above 400°C [25]. A study on the weldability of W showed that pre-heating to above the DBTT is needed to eliminate cracking in pure W parts [26]. It also showed that multiple passes can greatly increase the extent of the cracking. Multiple passes are a necessary feature of the SLM process.

Literature reports on the successful production of W parts by SLM, but the reported densities are never higher than 90% and on average around 80% or lower [18, 27]. Because the main application of SLM W samples is in situations involving nuclear radiation, no structural load bearing capacity is needed, so little was said about the amount of porosity or possible cracking. The large volume of pores is likely to cause extensive stress relaxation and reduce or even eliminate cracking. In this research, the relative density of the W parts was around 98%. Because cracks appear when the temperature drops below the DBTT, there is only a small temperature range left over which residual stresss can build up again. Thus, the W parts are relatively stress free after removal from the base plate, indicated by the low stress in the top layer and low curl-up angle.

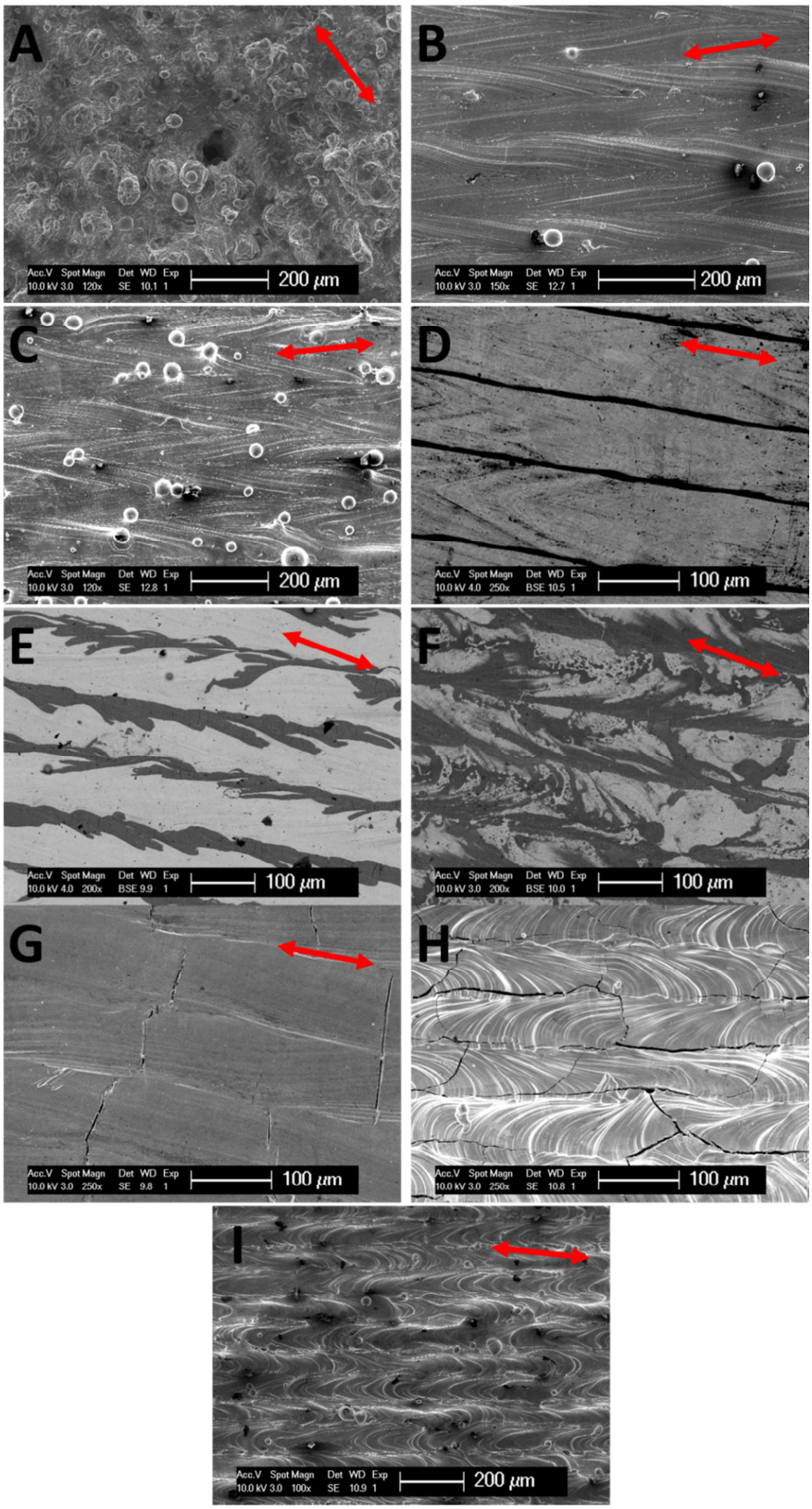

Figure 6 Top surfaces of the cube specimens. (A) AlSi10Mg. (B) Ti6Al4V-ELI. (C) Ti CP1. (D) 316L. (E) Maraging 18Ni300. (F) Inconel718. (G) Hastelloy C-276. (H) W. (I) Ta.

Next to W, the Hastelloy C-276 parts are also heavily cracked. The cracks are oriented perpendicular to the scan tracks. While the cracks in W are likely caused by a DBTT that lies above room temperature, Hastelloy C-276 is an FCC material and does not have a DBT. Transversal cracks in welds are less common than longitudinal cracks and are caused by the residual stresses in the longitudinal direction of the weld. The directional anisotropy of the residual stresses is already discussed above. The exact moment that these cracks occur is likely located at higher temperatures than the nucleation of cracks in W. The residual stress at room temperature and the curl-up are considerably higher for Hastelloy C-276 than for W.

Another less likely reason that could lead to cracks in SLM Hastelloy C-276 parts is a phenomenon called ductility dip cracking or DDC. DDC is a type of hot cracking that occurs for materials that experience a sudden drop in ductility over a certain temperature range. Ni-Cr based alloys are particularly prone to this type of cracking [28, 29]. The mechanism involves the precipitation of $M_{23}C_6$ carbides at grain boundaries. This precipitation requires some time to complete, time that is not available during SLM in which cooling rates above 10^6 °C/s are reached. Furthermore, Inconel 718 is also very susceptible to this phenomenon but does not show cracking during processing by SLM.

The reason why Hastelloy C-276 and W do show cracking and other materials such as Inconel 718 and Ta do not is unknown. In Table 1, there are no material properties that set it apart from all the other materials studied in this research. It is possible that other more advanced properties such as the DBTT, grain boundary surface energies and high temperature mechanical behavior have some influence as well. This means that it is unlikely to find strong correlations between material properties and residual stresses. Possible solutions to eliminate cracking are preheating or alloying the material with suitable elements. These elements could, for example, raise the toughness or high temperature material properties, lower the DBTT or lower the thermal expansion coefficient, much like Si does in Al alloys.

Oxide formation

The top surface of 316L, Inconel 718 and maraging steel all show oxide formation, as is clear from Figure 6D-F. The appearance and morphology of the oxide layer at the top of maraging steel SLM parts has been described by Thijs *et al.* [30]. It was found that the oxide layer consists of Al and Ti oxides, which is consistent with EDX measurements performed in this research, shown in Table 3. Furthermore, the maraging steel parts were built in a nitrogen atmosphere. The pickup of nitrogen also leads to the formation of TiN precipitates.

Table 3 Composition of the oxides on the top surface, as measured by point EDX measurements.

at%	*O*	*Ti*	*Al*	*Fe*	*Ni*	*Cr*	*Rest*
316L oxides	69	-	-	5	1	7	11 Si, 7 Mn
Inconel 718 oxides	64	11	16	2	3	4	0
Maraging steel oxides	62	25	3	7	2	-	1 Co

The oxides in all three materials are predominantly present at the side edges of the scan track. For maraging steel and Inconel 718, the oxide layer also protrudes inwards toward the center of a track, and it does so following the contours of the melt pool. The reasons why the oxides are found at the edges of the melt pool are twofold. First, the driving force for oxidation is higher at lower temperature, which is at the periphery of the melt pool. Each metal-oxide system has an equilibrium temperature above which the oxide will dissolve. Combined with the extremely high cooling rates in SLM, Thijs *et al*. [30] state that no further oxidation will take place upon solidification and further cooling. Second, oxides are lighter than the molten metal and will drift to the top of the melt pool. The Marangoni flows in the melt pool are oriented outward at the top for low oxygen concentrations inside the melt. At higher oxygen levels, the flow direction changes and is oriented inward [31].

The oxides are present on top of each layer when it has just been scanned and is broken up when a new layer is built on top, causing the oxides to break up. This can leave larger pieces of oxides entrapped in the part. The result is a dispersion of oxide particles in the steel matrix. The steel matrix has a larger thermal expansion coefficient than the oxides, resulting in a small gap between the matrix and the oxides. These oxides can then be considered equivalent to pores that change the surrounding residual stress state.

Conclusion

Nine different materials were investigated and compared via XRD stress measurements, deformations of bridge-shaped specimens and FE calculations. Several phenomena, such as micro-cracking and the formation of oxides were found to have an important effect on the final residual stress state. The influence of material properties on the buildup of residual stress is obscured by the several different phenomena at play. Future research will focus on the influence of the individual process parameters.

Acknowledgements

Research funded by a Ph.D. grant of the Agency for Innovation by Science and Technology (IWT). Partial financial support is also appreciated from KULeuven GOA/10/12.

References

[1] Kruth JP, Levy G, Klocke F, Childs THC. Consolidation phenomena in laser and powder-bed based layered manufacturing. CIRP Ann-Manuf Technol 2007;56:730-59.
[2] Vasinonta A, Beuth J, Griffith ML. Process Maps for Controlling Residual Stress and Melt Pool Sizein Laser-Based SFF Processes. Proceedings of the Solid Freeform Fabrication Symposium 2000:200-8.
[3] Vasinonta A, Beuth J, Griffith ML. Process Maps for Predicting Residual Stress and Melt Pool Size in the Laser-Based Fabrication of Thin-Walled Structures. Journal of Manufacturing Science and Engineering 2007;129:101-9.
[4] Aggarangsi P, Beuth J, Griffith ML. Melt Pool Size and Stress Control for Laser-Based Deposition Near a Free Edge. Proceedings of the Solid Freeform Fabrication Symposium 2003:196-207.

[5] Zekovic S, Dwivedi R, Kovacevic R. Thermo-structural Finite Element Analysis of Direct Laser Metal Deposited Thin-Walled Structures. Proceedings of the Solid Freeform Fabrication Symposium 2005:338-55.
[6] Rangaswamy P, Griffith ML, Prime MB, Holden TM, Rogge RB, Edwards JM, et al. Residual stresses in LENS (R) components using neutron diffraction and contour method. Mater Sci Eng A-Struct Mater Prop Microstruct Process 2005;399:72-83.
[7] Moat RJ, Pinkerton AJ, Li L, Withers PJ, Preuss M. Residual stresses in laser direct metal deposited Waspaloy. Materials Science and Engineering: A 2011;528:2288-98.
[8] Klingbeil NW, Beuth J, Chin R, Amon C. measurement and modeling of residual stress-induced warpage in direct metal deposition processes. Proceedings of the Solid Freeform Fabrication Symposium 1998:367-74.
[9] Mercelis P, Kruth JP. Residual stresses in selective laser sintering and selective laser melting. Rapid Prototyping J 2006;12:254-65.
[10] Zaeh M, Branner G. Investigations on residual stresses and deformations in selective laser melting. Production Engineering 2010;4:35-45.
[11] Nickel AH, Barnett DM, Prinz FB. Thermal stresses and deposition patterns in layered manufacturing. Materials Science and Engineering: A 2001;317:59-64.
[12] Brückner F, Lepski D, Beyer E. Modeling the Influence of Process Parameters and Additional Heat Sources on Residual Stresses in Laser Cladding. J Therm Spray Technol 2007;16:355-73.
[13] Alimardani M, Toyserkani E, Huissoon JP, Paul CP. On the delamination and crack formation in a thin wall fabricated using laser solid freeform fabrication process: An experimentalâ€“numerical investigation. Opt Lasers Eng 2009;47:1160-8.
[14] Kruth JP, Deckers J, Yasa E, Wauthle R. Assessing and comparing influencing factors of residual stresses in selective laser melting using a novel analysis method. Proc Inst Mech Eng Part B-J Eng Manuf 2012;226:980-91.
[15] Internal database. LayerWise NV.
[16] Amato KN, Gaytan SM, Murr LE, Martinez E, Shindo PW, Hernandez J, et al. Microstructures and mechanical behavior of Inconel 718 fabricated by selective laser melting. Acta Mater 2012;60:2229-39.
[17] EOS. AlSi10Mg material data sheet. 2011.
[18] Hastelloy C-276 alloy information. Haynes International.
[19] Thijs L, Kempen K, Kruth J-P, Van Humbeeck J. Fine-structured aluminium products with controllable texture by selective laser melting of pre-alloyed AlSi10Mg powder. Acta Mater 2013.
[20] Thijs L, Montero Sistiaga ML, Wauthle R, Xie Q, Kruth J-P, Van Humbeeck J. Strong morphological and crystallographic texture and resulting yield strength anisotropy in selective laser melted Ta. Acta Mater 2013;61:4657-68.
[21] Thijs L, Verhaeghe F, Craeghs T, Van Humbeeck J, Kruth JP. A study of the micro structural evolution during selective laser melting of Ti-6Al-4V. Acta Mater 2010;58:3303-12.
[22] Murr LE, Quinones SA, Gaytan SM, Lopez MI, Rodela A, Martinez EY, et al. Microstructure and mechanical behavior of Ti-6Al-4V produced by rapid-layer manufacturing, for biomedical applications. Journal of the Mechanical Behavior of Biomedical Materials 2009;2:20-32.
[23] Kelly S, Kampe S. Microstructural evolution in laser-deposited multilayer Ti-6Al-4V builds: Part I. Microstructural characterization. Metall Mater Trans A 2004;35:1861-7.

[24] Dieter GE. Chapter 15: Residual Stresses. Mechanical Metallurgy. 3rd ed. New York: McGraw-Hill; 1961.
[25] Material database. LayerWise NV.
[26] Cole N, Gilliland R, Slaughter G. Weldability of W and its alloys: Defense Technical Information Center.; 1968.
[27] Deprez K, Vandenberghe S, Van Audenhaege K, Van Vaerenbergh J, Van Holen R. Rapid additive manufacturing of MR compatible multipinhole collimators with selective laser melting of W powder. Med Phys 2013;40.
[28] Lippold JC, Nissley NE. Ductility-dip cracking in high chromium, Ni-base filler metals. Hot Cracking Phenomena in Welds II: Springer; 2008. p. 409-25.
[29] Young GA, Capobianco TE, Penik MA, Morris BW, McGee JJ. The mechanism of ductility dip cracking in nickel-chromium alloys. WELDING JOURNAL-NEW YORK- 2008;87:31.
[30] Thijs L, Van Humbeeck J, Kempen K, Yasa E, Kruth J-P, Rombouts M. Investigation on the inclusions in maraging steel produced by selective laser melting. Innovative Developments in Virtual and Physical Prototyping 2012:297-304.
[31] Lu SP, Fujii H, Nogi K. Marangoni convection and weld shape variations in Ar-O-2 and Ar-CO2 shielded GTA welding. Mater Sci Eng A-Struct Mater Prop Microstruct Process 2004;380:290-7.